Ceramics International 50 (2024) 29568–29579

Contents lists available at ScienceDirect

Ceramics International

journal homepage: www.elsevier.com/locate/ceramint

Unraveling the morphology-structure-property relationship of silver orthovanadate p-semiconductor: Experimental and theoretical investigation

Guilherme Henrique Cruvinel [a], Regiane Cristina de Oliveira [a], Marisa Carvalho de Oliveira [a], Ivo Mateus Pinatti [b,**], Renan Augusto Pontes Ribeiro [c], Elson Longo [a,*]

[a] Functional Materials Development Center, Federal University of São Carlos, UFSCar, São Carlos, São Paulo, Brazil
[b] Department of Chemistry, Federal University of Maranhão, Av. dos Portugueses, 1966, São Luís, MA, 65080-805, Brazil
[c] Department of Natural and Earth Sciences, State University of Minas Gerais, Av. Paraná, 3001, 35501-170, Divinópolis, MG, Brazil

ARTICLE INFO

Handling Editor: P. Vincenzini

Keywords:
Semiconductor
Ag_3VO_4
Microwave-assisted hydrothermal synthesis
Vanadate
DFT simulations

ABSTRACT

Silver vanadate (Ag_3VO_4) is considered one of the most important semiconductors. It finds practical applications in electrochemical cells, as bactericidal and virucidal agents, in photocatalysis, and environmental remediation. Despite the impressive experimental progress, the dependence of the properties of a material is strongly linked to its chemical composition and structure. In this sense, the peculiar physical-chemical properties of the vanadate's class have become important. However, the fundamentals of structure in this material remain poorly understood, and the theoretical insight into the morphology linked to its properties is completely missing. In the present study, different synthesis times were tested in the obtention of Ag_3VO_4 crystals by the microwave-assisted hydrothermal method, and their properties were discussed based on experimental results and quantum mechanics simulations. Structural characterizations (XRD, Raman and UV–vis spectroscopy, FE-SEM, and TEM analyses) confirmed the material order at short, medium, and long-range. Theoretical calculations contributed to identifying the atom distribution in the structure, nature of the type of electronic transition, and density of states present in the valence and conduction bands. The topological analysis of the electron density indicated transit chemical interactions and unexpected argentophilic interactions, and Mulliken, Hirshfeld and Bader population analysis provided the charges present on the chemical elements of the crystal. Predicted theoretical surface shapes and their stabilities were evaluated along with FE-SEM images.

1. Introduction

Alternative routes for the synthesis of materials whose energy and time demands are relatively smaller have been the object of constant study by researchers. The microwave-assisted hydrothermal method has gained evidence in recent years due to its compliance with these characteristics, which leads to greater savings and contribution to the environment compared to traditional methods [1,2]. Microwaves may be used to improve photocatalytic activity, soil sterilization, cutting blood vessels, heterogeneous catalysis, synthesis of nanomaterials, and induce morphology changes in particles, among other applications [2–13].

The dependence of the properties of a material is strongly linked to its chemical composition and structure. In this sense, the peculiar physical-chemical properties of the silver orthovanadate (Ag_3VO_4) and its composites are drawn important attention to practical applications, such as optoelectronic and solar energy conversion, photoelectrochemical biosensor, photocatalytic degradation and electrochemical detection of organic compounds, removal of different wastewater pollutants, dye degradation, antibiotics degradation, phenol degradation and heavy metal ions reduction [14–18]. Numerous semiconductors and other catalysts, including TiO_2 and its composites, ZnO, Pd/C_3N_4, Pt/C_3N_4, acidic MIL-125, BP–UiO [19–26], have undergone extensive study. However, regarding semiconductors, they encounter challenges like wide bandgaps and low photodegradation rates when exposed to visible light [14]. Silver orthovanadate (Ag_3VO_4) emerges as

* Corresponding author.
** Corresponding author.
E-mail addresses: ivo.pinatti@ufma.br (I.M. Pinatti), elson.liec@gmail.com (E. Longo).

https://doi.org/10.1016/j.ceramint.2024.05.252
Received 4 January 2024; Received in revised form 22 April 2024; Accepted 16 May 2024
Available online 17 May 2024

a promising solar-driven semiconductor with a suitable bandgap (~2.20 eV) and is recognized for being a green semiconductor [14,27,28].

Among metal vanadates, silver orthovanadate emerges as a p-type semiconductor which has 3 polymorphs: the α, β and γ-phase [29–33]. The α-phase can be obtained at room temperature with a monoclinic crystalline structure and *C*2/*c* space group, which is not observed in AB_3X_4 systems [31]; at temperatures from 110 °C to 414 °C, the β-phase with tetragonal crystalline structure and $I\,\overline{4}\,2\,m$ space group is obtained; and between 414 °C and 530 °C, the γ-phase with a cubic crystalline structure and $F\,\overline{4}\,3\,m$ space group is obtained [29,31]. There is no breaking of chemical bonds in the phase transition processes among the α and β phases, and the β and γ phases. Instead, only a rearrangement of atoms within the structure occurs. Therefore, these phase transitions are reversible. [29,31], and are known as displacive [34].

According to *Vali* et al. [29], few research were carried out to understand the structural and theoretical characteristics of silver orthovanadate, which could improve the understanding of the processes involved in its photocatalytic and other applications. *Pan* et al. [35] and *Liao* et al. [36] synthesized Ag_3VO_4 by microwaves-assisted hydrothermal method using different reagents and synthesis parameters, but temporal effect of microwaves irradiation on Ag_3VO_4 structure was not evaluated. Both studies were focused in producing silver orthovanadate to verify its photocatalytic activity, which the former made correlations in morphology, surface hydroxyl groups, and the surface acidity of samples. Additionally, structural and morphological changes could be observed in materials, as $ZnWO_4$ and $Ce_2(MoO_4)_3$, synthesized by microwaves-assisted hydrothermal method in different synthesis time (less than 120 min) [37,38]. These studies showed synthesis time in microwaves-assisted hydrothermal method is able to result in different crystallite size, crystallinity, cell unit parameters and medium-range structural modifications. *Oliveira* et al. [39] observed α-$AgVO_3$ – another silver vanadate's phase - is susceptible to morphological modifications due to small temperature changes.

In this sense, this study evaluates Ag_3VO_4 samples synthesized using the microwave-assisted hydrothermal (MAH) route in different synthesis times. *Ab initio* quantum-mechanical calculations were performed to provide an in-depth atomic-level comprehension of structural, electronic, and vibrational properties along with experimental characterization. Moreover, charges and their distributions as well as chemical interactions and its character existing in Ag_3VO_4 were calculated and analyzed. Finally, theoretical investigations were carried out to understand the contribution of Ag_3VO_4 surfaces on crystal morphology, and these findings were subsequently compared to the observed experimental morphologies.

2. Experimental procedure

2.1. Synthesis

Ag_3VO_4 crystals (Solubility product: K_{sp}: 10^{-24} [40]) were synthesized as follow: 3 mmol of sodium orthovanadate (Na_3VO_4) (99.98 %, Sigma-Aldrich; Solubility: soluble [41]) and 9 mmol of silver nitrate $AgNO_3$ (99.00 %, Cennabras; Solubility: 257 g/(100 mL H_2O) at 25 °C [42]) were separately dissolved in 60 mL of distilled water under magnetic stirring at room temperature for 5 min. The solution containing the Ag^+ ions was added to the $[VO_4]^{3-}$ ions solution, and the resulting system was maintained under magnetic stirring for 15 min. The combination of the two solutions allows the immediate formation of a yellow-orange precipitate through the binding between Ag^+ and $[VO_4]^{3-}$ ions driven by a low solubility product of silver orthovanadate. Afterwards, the suspension was submitted to MAH system with a heating rate of 30 °C/min, and a time plateau for different synthesis times: 2^x (x: 1, 2, 3, 4, 5 and 6) min, at 120 °C. The samples were collected at room temperature, washed 5 times with distilled water and dried in a conventional furnace at 60 °C for 24 h. All the chemical reactions and physical transformations are described below.

$$Na_3VO_4 \rightarrow 3Na^+ + [VO_4]^{3-}$$

$$AgNO_3 \rightarrow Ag^+ + [NO_3]^-$$

$$3Ag^+ + [VO_4]^{3-} \rightleftharpoons \alpha - Ag_3VO_4$$

$$\alpha - Ag_3VO_4 \rightleftharpoons \beta - Ag_3VO_4$$

2.2. Characterization

All samples were structurally characterized by a Rigaku X-Ray Diffractometer, model D*Max*2500PC, Japan (Cu-Kα radiation; λ = 1.5406 Å). Scanning in the 2θ range from 10° to 110° was employed. The diffraction patterns of the powders were compared with the diffraction patterns according to the crystallographic form ICSD (Inorganic Crystal Structure Data) with No.: 417469 referring to the Ag_3VO_4 material (monoclinic structure) [43]. To obtain details of the long-range structure, the Rietveld refinement was performed using the GSAS-II (General Structure Analysis System) software [44]. For the refinement of the samples in this work, the structure No.: 417469 from the ICSD database was used as a starting model. The material was morphologically characterized by means of scanning electron microscopy with a field emission gun (FEG-SEM), using the Carl Zeiss equipment (Germany), model Supra 35-VP and by transmission electron microscopy (TEM), using a FEI (model Tecnai G^2 F20, USA) microscope. Raman spectroscopy (micro-Raman) measurements were performed at room temperature, range from 50 to 1200 cm^{-1}, using a Micro-Raman iHR550 spectrometer (Horiba Jobin-Yvon, Japan), coupled with a CCD detector and equipped with a He–Ne laser (Melles Griot, USA) operated at excitation source of λ = 633 nm and a maximum power of 200 mW. Measurements by ultraviolet–visible diffuse reflectance spectroscopy (UV–Vis) of silver orthovanadate powders were carried out using a Varian spectrophotometer (USA), model Cary 5G, at room temperature.

2.3. Computational details

The structural, electronic, vibrational and topological properties of α-Ag_3VO_4 were investigated using quantum mechanical calculations within the density functional theory with hybrid functional B3LYP [45,46] improved by interactions of Grimme-D3 dispersion [47] as implemented in the CRYSTAL17 code [48]. The basis set of all electrons 8-411d1 was used for oxygen, 86-411d4G for V, and the Hay-Wadt small nucleus pseudopotentials (HAYWSC) 311d31G for Ag [49–51]. Electronic integration over the Brillouin Zone (ZB) was performed using a 6 × 6 × 6 Monkhorst-Pack k-point mesh [52]. Set of five bounds (ITOL) defined for 8, 8, 8, 8 and 14 controlled the accuracy of Coulomb calculations and shift integrals according to overlap criteria, i.e. when the overlap between two atomic orbitals is less than 10^{-ITOL} (10^{-8}, 10^{-8}, 10^{-8}, 10^{-8}, 10^{-16}). The self-consistent field (SCF) convergence limit at full energy was set to 10^{-8} Hartree, while mean square (RMS) gradient, RMS shift, maximum gradient, and maximum shift were set to 3.10^{-4}, $1.2.10^{-3}$ $4.5.10^{-4}$ and $1.8.10^{-3}$ a.u., respectively. The cif file used for the geometry optimization was produced by the Rietveld method from the silver orthovanadate sample synthesized for 64 min.

The vibrational frequencies at the Γ-point with harmonic approximation were calculated for the optimized geometry by diagonalizing the mass-weighted Hessian matrix, while the relative Raman intensities for polycrystalline powders were calculated by exploiting the orbital energy-weighted density matrix based on the self-consistent solution of Equations for First and Second Order Perturbed Coupled Hartree-Fock/Kohn-Sham (CPHF/KS) for the electronic response to external electric fields in equilibrium geometry [53–55]. In addition, the electronic properties were evaluated through the band gap value and the density of states (DOS) obtained in the CRYSTAL17 code [48]. To identify and

evaluate the nature of the chemical interactions between the atoms belonging to the structure, the topological analysis of the electronic density $\rho(r)$ was obtained using the TOPOND code [56]. To achieve this objective, critical points (3, −1) were analyzed, which correspond to connections in a crystal in Bader's theory [57]. To obtain an analysis of the charge distribution on the atoms present in the structure, different methods (Mulliken, Hirshfeld and Bader) were combined with two-dimensional electron density difference map.

Aiming to evaluate the role of Ag_3VO_4 surfaces on the crystal morphology, the (100), (010), (001), (101), (110), (011), and (111) surfaces were modeled considering different surface terminations of each orientation, as depicted in Fig. S8. The surface stability was investigated using a thermodynamic approach [58,59], where the surface energy (γ) of the specific surface termination is defined as:

$$\gamma = \frac{1}{2A}\left(E_{slab} - \sum_i N_i \mu_i\right) \quad (1)$$

where E_{slab} is the total energy per unit cell of the slab in the (hkl) direction slab; N_i is the numbers of (i) species that compose the slab (Ag, V, and O atoms); μ_i are the chemical potentials of (i) constituents, and A is the surface area of slab unit cell. Due to the thermodynamic equilibrium between the slab termination and the bulk, the chemical potentials of Ag, V, and O atoms are conditioned to a range in which Ag_3VO_4 bulk is stable:

$$3\mu_{Ag} + \mu_V + 4\mu_O = E_{Ag_3VO_4} \quad (2)$$

$$\Delta\mu_{Ag} = \mu_{Ag} - E_{Ag} \quad (3)$$

$$\Delta\mu_V = \mu_V - E_V \quad (4)$$

$$\Delta\mu_O = \mu_O - \frac{1}{2}E_{O_2} \quad (5)$$

Here, E_{Ag}, E_V, and E_{O_2} are the total energy of metallic Ag and V bulk, and O in gaseous molecular O_2 in the triplet state, respectively, and $\Delta\mu_{Ag}$, $\Delta\mu_V$, and $\Delta\mu_O$ refer to the difference of chemical potential in the slab and metallic bulk (Ag and V) or gas phase (O_2), at 0 K and 1 bar.

The total energy of metallic Ag and V bulk were obtained using the definition of the Gibbs energies of formation for the binary oxides Ag_2O and V_2O_5:

$$E_M = \frac{1}{x}\left[E_{M_xO_y} - \Delta G^{\circ}_{f\ M_xO_y} - \frac{y}{2}\left(E_{O_2} + \Delta G^{gas}_{O_2}(T^{\circ}, p^{\circ})\right)\right] \quad (6)$$

where $\Delta G^{\circ}_{f\ M_xO_y}$ is the Gibbs energy of formation for oxide (Ag_2O and V_2O_5) under the standard conditions available from thermodynamic tables; $E_{M_xO_y}$ is the total energy of M_xO_y oxide (per unit cell) and $\Delta G^{gas}_{O_2}(T^{\circ}, p^{\circ})$ is the change of the Gibbs energy of oxygen gas from 0K to the standard conditions [59].

The range of values of the chemical potentials which consistent with existence and stability of the crystal, is determined by the set of the following conditions:

$$\Delta\mu_{Ag} < 0 \quad (7)$$

$$3\Delta\mu_{Ag} + 4\Delta\mu_O > \Delta G^{bulk}_{f\ Ag_3VO_4} \quad (8)$$

$$2\Delta\mu_{Ag} + \Delta\mu_O < \Delta G^{bulk}_{f\ Ag_2O} \quad (9)$$

$$6\Delta\mu_{Ag} + 3\Delta\mu_O > 2\Delta G^{bulk}_{f\ Ag_3VO_4} - \Delta G^{bulk}_{f\ V_2O_5} \quad (10)$$

This procedure is important because the oxygen chemical potential dependence can be associated with the external Temperature and pressure using the ideal-gas-like behavior and the thermodynamic data reported in the NIST Chemistry WebBook [60].

Furthermore, the crystal morphology was predicted considering the Wulff Construction for different chemical potentials through the surface energy values for the (100), (010), (001), (101), (110), (011), and (111) surfaces, as conducted in previous works [61–63]. In particular, the theoretical morphologies were build using VESTA [64].

3. Results and discussion

3.1. Structural analysis

X-ray diffraction and Rietveld refinement were performed to obtain information on the structure long-range order of the materials synthesized for different times. Fig. 1 shows the diffractograms for the synthesized samples. In Fig. S1 are the refinement patterns, and Table S1 shows the values of the R_{wp} (weighted-profile R - factor), R_f^2 (unweighted single-crystal R-factor), S (goodness-of-fit) and reduced χ^2 (S^2) parameters, which indicate the quality of the refinements. The difference between the observed and calculated patterns, as well as the quantitative parameters, show that the refinements performed are adequate.

All diffraction patterns of silver orthovanadate samples displayed in Fig. 1 are in accordance with crystallographic card No. 417469 (Inorganic Crystal Structure Database - ICSD), which refers to monoclinic structure and *C*2/*c* spatial group [31,32]. This result indicates that there was no formation of secondary phases, and the narrow and well-defined peaks indicate that there is high structure long-range order. According to Table S2, the cell parameters do not change significantly among samples. The samples show higher volume values than the crystallographic card, and it suggests unit cell expansion for the samples synthesized using this methodology.

The synthesis conditions used can generate heterogeneity in the samples. According to *Horikoshi and Serpone* [5], increasing the temperature and the presence of ions play an important role in the penetration of microwave radiation in the reaction system, whose temperature increase acts allowing a greater penetration in liquid water, while the presence of free ions has the opposite effect. At 90 °C, this work provides that the penetration of microwave radiation reaches 5.4 cm in liquid water, while when adding 0.25 M of NaCl, the penetration range decreases to 0.4 cm [5]. Considering the reaction cell (diameter: 4.3 cm) and the presence of ions in the solution, it is reasonable to consider the presence of thermal gradients. In addition, there is no addition of a compound that allows electrostatic or steric stabilization in the synthesis, which does not allow a controllable growth mechanism [65–68]. Additionally, there is phase transformation from α to β-phase during heating (110 °C) [29,31]. Such conditions and other factors can contribute to generating heterogeneities in the sample structures, such as the presence of microstrain, which can be generated by thermal contractions, vacancies, expansions, etc [69]. Data presented in Table S2

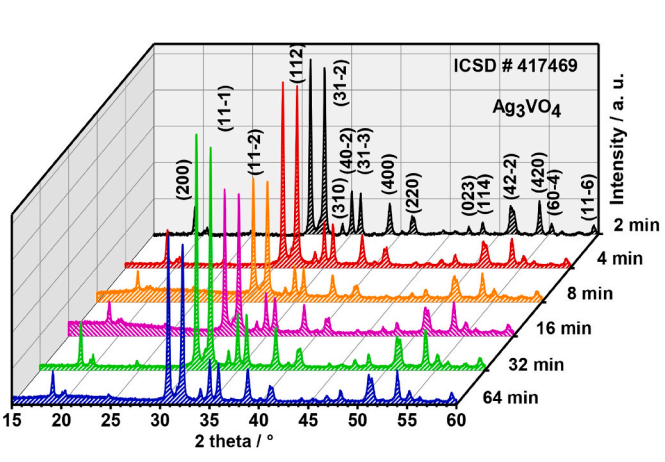

Fig. 1. XRD patterns of Ag_3VO_4 obtained by MAH method.

suggest the microstrain presence and indicate the degree of tension relief in samples synthesized for 32 and 64 min. The synthesis time apparently did not cause significant changes in the average crystallite size, whose values comprise values between 53 and 65 nm.

Theoretical calculations were performed to characterize the Ag_3VO_4 structure. Three types of clusters are presented in the monoclinic structure of silver orthovanadate composed by V, Ag and O atoms: one $[VO_4]$ cluster, and two $[AgO_4]$ clusters, whose metallic elements are coordinated by four oxygen atoms. According to literature [31,32], the $[VO_4]$ cluster have a tetrahedral structure and the $[AgO_4]$ clusters have a pseudo seesaw coordination $[Ag_SO_4]$ polyhedron and distorted square planar $[Ag_PO_4]$ polyhedron. According to theoretical results the $[Ag_SO_4]$ distorted seesaw structure has four different chemical bonding and $[Ag_PO_4]$ distorted square planar and $[VO_4]$ distorted tetrahedral structures have two different chemical bonding (see Fig. 2 and S2). The chemical bond distances between silver and oxygen atoms are longer than the distances between vanadium and oxygen atoms. The distortions presented in clusters or coordination polyhedra can lead to different deformations in chemical bonds, which can influence the properties of the material [70]. The cell parameters optimized by DFT are presented in Table S2 and Fig. S2, which are in agreement with the experimental results obtained by Rietveld refinement.

In Fig. 3, the normalized Raman spectra for the synthesized Ag_3VO_4 samples are shown, and the theoretical and experimental wavenumber of Raman-active vibrational modes are given in Table S4. The α-phase silver orthovanadate [31,32] present 21 active Raman modes, which can be determined by the following irreducible representations at Γ point of the Brillouin zone:

$$\Gamma = 10A_g + 11B_g \tag{11}$$

It is noticed in Fig. 3 that all the spectra present 10 active Raman modes. In addition, it is possible to note that the vibrational modes are broad, which may suggest structure short-range disorder. It indicates that may occur difference in the average size of crystals or in the strength of interaction between the constituent species [70], as well as the insertion of defects and stresses in the lattice [71–73], which may be a result of synthesis method. Also, line broadening may also be caused by local heating due to the laser equipment, especially in temperature-sensitive materials like silver-based oxides. So, this similarity among spectra reveals that the time parameter does not imprint significant changes in the structure short-range. These spectra slightly may differ from other spectra produced by other synthesis methods (e.g. peak shift, band broadening, relative intensity, etc), such as those found by *Vali* et al. [29] and *Zaki* et al. [74].

Figure S3 **a)** shows the normalized Raman spectra for the Ag_3VO_4 samples synthesized at 2 min and 64 min and theoretical Raman spectrum, while Figure S3 b) shows the experimental and calculated Raman-active modes. The theoretical peaks assigned to the experimental ones are at 63.88, 87.61, 193.76, 240.76, 325.01, 791.86 and 827.60 cm^{-1}. The peaks related to smaller wavenumber up to 325.01 cm^{-1} correspond to different types of vibrations (twisting, rocking, bending and stretching) involving V–O bonds of $[VO_4]$ cluster, and Ag–O bonds of $[Ag_SO_4]$ cluster, whose vibration frequencies involve complex and coordinates atomic vibrations in this material. Above 325.01 cm^{-1}, it is noted there is a decrease in the active contribution of Ag atoms to atomic vibration. A good agreement between theoretical and experimental data is seen in Figure S3 b).

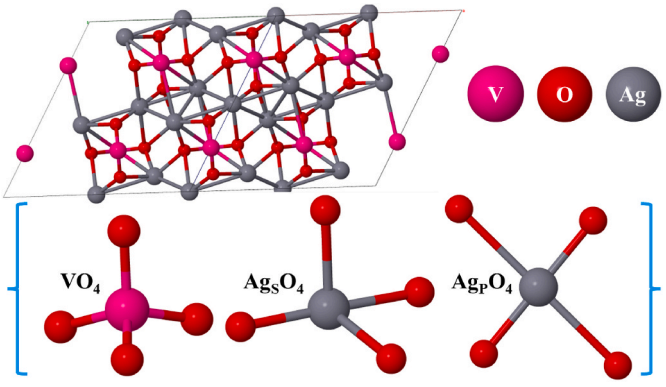

Fig. 2. Schematic representation of optimized monoclinic crystalline structure of Ag_3VO_4 and its coordination polyhedra. Vanadium, oxygen and silver atoms are represented by pink, red and gray colors, respectively. (For interpretation of the references to color in this figure legend, the reader is referred to the Web version of this article.)

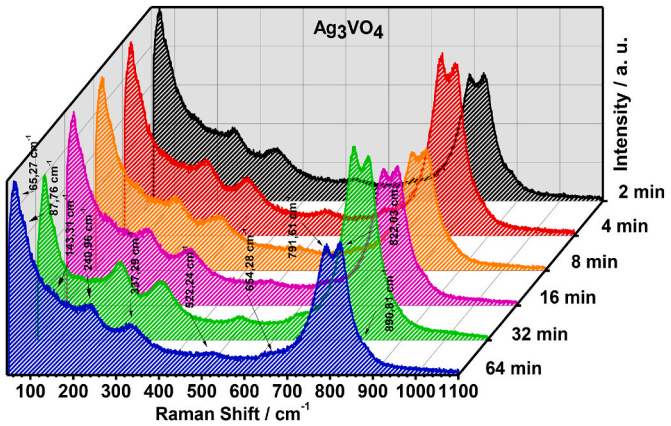

Fig. 3. Experimental Raman spectra of Ag_3VO_4 obtained by MAH method.

According to Aouadi et al. [75], the literature lacks Raman data for phases of silver vanadate, whose Raman modes assignments are made based on other materials (e. g. other vanadates [29,70,76–81] – see Table S5). Based on these theoretical results, the experimental Raman modes can be mainly attributed to: i) twisting and rocking vibrations in $[VO_4]$ polyhedra and in $[Ag_SO_4]$ cluster with the contribution of Ag cations translation modes at 65.27 cm^{-1}; ii) bending vibrations in $[VO_4]$ and $[Ag_SO_4]$ clusters with the contribution of Ag cations translation modes at 87.76 cm^{-1}; iii) bending and symmetric stretching at 143.31 cm^{-1} in $[Ag_SO_4]$ cluster with the contribution of Ag cations translation modes; iv) rocking vibrations in $[VO_4]$ polyhedra and bending and asymmetric stretching vibrations in $[Ag_SO_4]$ polyhedral with the contribution of Ag cations translation modes at 240.96 cm^{-1};v) bending and twisting vibrations in the V–O bonds of $[VO_4]$ clusters at 337.29; asymmetrical stretching and wagging vibrations and symmetric stretching vibrations in $[VO_4]$ clusters at 791.61 and 822.03 cm^{-1} respectively.

3.2. Optical and electronic analyses

Fig. S4 shows the UV–vis diffuse reflectance spectra of the samples. The samples showed absorption in the visible range at approximately 580 nm. All of them reveal the presence of the Urbach tail [82], which contributes to electronic structure analysis of the materials. Silver orthovanadate is a p-type semiconductor [29,33], i.e., presents electron deficits which electronic levels below the Fermi level and above the valence band, called acceptor levels, favoring the conduction mainly through holes [83]. In other words, Ag_3VO_4 has an intrinsically defective electronic structure, which naturally contributes to produce the Urbach tail. Additionally, *Trimarchi* et al. [33] showed that, due to the tendency to form weaker chemical bonds between Ag and O atoms, Ag vacancy formation is energetically more favorable in Ag_3VO_4. So, it is reasonable to state that the formation of the "tail" in all samples can suffer a contribution and be related to the presence of electronic levels produced by Ag vacancies and other changes provided by synthesis method.

Energy gap (E_{gap}) of the samples were calculated and are presented in Fig. S5, considering both direct (n = 1/2) and indirect (n = 2) electronic transitions [84–87]. It is verified that there is a variation in the Tauc plots when considering the direct band-gap, whose values range from 2.33 eV (64 min) to 2.41 ev (2 min); and from 2.09 eV (8 min and 32 min) to 2.13 eV (4 min) considering indirect energy band-gap (Table S6). These results suggest that there is no significant changes in the optical band-gap considering variation synthesis parameter (time). However, MAH method may produce a different electronic structure when compared to other synthesis methods reported in the literature. Moreover, the experimental results fit within the experimental values reported in the literature assuming intermediate positions in the range from 2.05 eV to 2.58 eV considering a direct energy band-gap [29, 84–87] and from 2.18 eV to 2.37 eV for an indirect energy band-gap [29, 84]. These experimental estimated band-gap values are influenced by quantized size of the sample, doping, presence of functional groups on the surface, vacancies, thermal treatment, among other factors which can cause deviations of the values [88].

Ab initio simulations were performed to obtain information about the theoretical electronic structure. Band structure and atom-projected density of states were obtained (see Fig. 4 a)). As shown in Fig. 4 a), silver orthovanadate valence band (VB) is composed mainly by the contribution of electron levels of Ag and O atoms, while the vanadium atoms are mainly responsible for the formation of the conduction band (CB). This theoretical simulation indicates an indirect electronic transition from A1 (220) to A2 (330) and a band-gap energy equivalent to 2.41 eV, in agreement with the results obtained in the literature (see Table S6). The theoretical simulation of Ag_3VO_4 in *Peng* et al.'s work [89] showed that due to the partial overlap between the orbitals of oxygen and silver atoms, the chemical bonding energy between these atoms is weaker than for V–O, which may explain process of photocorrosion through the existence of silver vacancies.

Fig. 4 b) and c) show the band structure and the projected density of projected states in silver atoms, considering all silver atoms in a unit cell (6 atoms) and only non-equivalent silver atoms (Ag_S and Ag_P), respectively. It was observed that silver atoms belonging to the see-saw coordination polyhedron have a greater contribution in the uppermost VB, due to its higher amount (4 atoms) presence in this structure. In Fig. 4 c), it is expected to verify the individual contribution of different silver atoms in the electronic band structure. Although there are non-equivalent silver atoms in the structure, it is noted that there is no significant difference in the contribution to the intensity in the density of states closer to the VB maximum.

To evaluate the nature of the chemical bond between atoms and their electronic density in the lattice, analysis of the electronic charge distribution using different methods (Mulliken, Hirshfeld and Bader), 2D charge density difference map and charge density topological analysis were performed. The results are listed in Table 1, which show that silver atoms have a similar electrical charge with values between +0.600 and + 0.700 (in absolute values), even considering that these atoms belong to different coordination polyhedra and have different chemical bond distances. Also, despite the considered methods, it revealed that changing the atomic arrangement in space did not cause significant influence on the charges. The same behavior is observed for oxygen atoms, whose charge values are between −0.970 and −1.100 (in absolute values), and vanadium atoms that exhibits charges between +2.000 and + 2.210 (in absolute values). These results indicate a partially ionic nature of the chemical bonds present in this structure, and the values presented by the different methods are in good agreement with each other. Also, it is important to highlight that the obtained atomic charges do not follow the expected formal charges (Ag^{1+}, V^{5+} and O^{2-}) confirming the quantum nature of Ag–O and V–O chemical bonds that contributes to spread the electron density over all atoms, which can be associated with the transit character of chemical bonds in the viewpoint of Bader theory [57].

Table 1
Hirshfeld (eH), Mulliken and Bader (eB) charges (in absolute values) calculated for the non-equivalent atoms Ag, V and O (1 and 2) in a see-saw coordination polyhedron (Ag_SO_4), square planar (Ag_PO_4) and tetrahedra (VO_4).

Ag_3VO_4	e_H	Mulliken	e_B
Ag_S	+0.615	+0.653	+0.682
Ag_P	+0.605	+0.671	+0.672
V	+2.136	+2.031	+2.208
O(1)	−1.007	−1.001	−1.060
O(2)	−0.979	−1.003	−1.062

The 2D charge density difference map (Fig. S6) shows the charge density difference between an isolated atom and its corresponding ion. It can be seen that, as expected, the vanadium cations are represented on the map by areas in blue (ρ_V (ion) - ρ_V (atom) < 0), as well as the silver cations (ρ_{Ag} (ion) - ρ_{Ag} (atom) < 0. In this case, the charge transfer is carried out to the oxygen atoms, which are represented by the red areas. Oxygen atoms undergo a reduction process to form the Ag_3VO_4 structure. Such results converge with the results shown in Table 1, referring to the atomic charge of this structure.

Electron density, laplacian, virial density and degree of chemical bonding at the critical point were analyzed for silver orthovanadate according to the procedure described by *Gatti* [90]. These data are listed in Table S7 which shows that all chemical interactions present in silver orthovanadate are classified as transit (intermediate), which means they can not be classified as purely ionic or covalent. Table 1 showed that chemical bonds have a partially ionic nature. Although, the chemical bonds between the V and O atoms are classified as transit, these bonds have the highest electron densities and the highest |V|/G and bond degree at the critical point, which shows that chemical bonds have a higher degree of covalence than interactions between oxygen and silver atoms.

In addition, these results allow show that there is a chemical interaction between silver atoms of different coordination polyhedra (Ag_S–Ag_P: 3.074 Å) and the same (Ag_S–Ag_S: 3.016 Å) in Ag_3VO_4. Considering the chemical interactions between silver and oxygen atoms, it is noted that the electron density increases when the distance from the chemical bond is reduced, which increases the degree of covalence of the

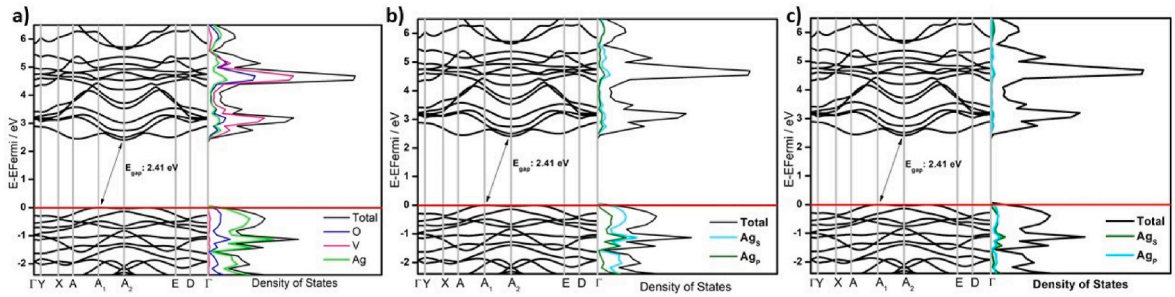

Fig. 4. Band structure and density of states projected in: a) all atoms (16 atoms per cell); b) all silver atoms (6 atoms per cell); c) all non-equivalent silver atoms (Ag_S: 4 and Ag_P: 2 atoms per cell) for Ag_3VO_4.

chemical bond, but does not show significant changes between these interactions, even considering different silver atoms. The same behavior is observed in chemical interactions between silver atoms (Ag_S–Ag_S and Ag_S–Ag_P) and between oxygen and vanadium atoms (V–O). As already mentioned, the nature of the chemical bond between oxygen and silver atoms is more ionic and does not show significant differences between them, even considering different silver coordination polyhedra. However, the structure of silver orthovanadate allows interactions between silver atoms from different and equal coordination polyhedra.

In Fig. 5 is the optimized crystal structure containing silver and oxygen atoms. Considering this structure, it is noted that although there are several silver atoms, the most far-reaching chemical interactions between the silver atoms must occur at the smallest distances between the Ag_S atoms (Ag_S–Ag_S: 3.016 Å) and between the Ag_S and Ag_P atoms (Ag_S–Ag_P: 3.074 Å). It is important to mention that such interactions are limited to certain distances, which limits the number of chemical interactions between a specific silver atom and other nearby silver atoms.

It is showed that interactions between chemical species of the same charge play a fundamental role in stabilizing the formation of crystals, and the interactions are not rare or errors in theoretical chemistry simulations [91]. The study of Korabel'nikov and Zhuravlev [92] detected the presence of weak interactions between anions in many oxyionic crystals. Chemical interactions between cations and anions can lead to the formation of ionic crystals, whose interactions between cations and between anions are repulsive or non-existent according to classical theoretical chemistry [91]. In some crystals, anions can become closer, which could be explained by the presence of small cations that force large anions to approach [93]. However, this approach is based on the consideration of the stability study of the approximation of anions in the gaseous phase, which results in instability [94]. These results represent important aspects in the properties and stability of these materials, as the process of formation of silver nanoparticles through the silver vacancy mechanism associated with the irradiation with an electron beam and laser and, consequently, their applications.

3.3. Surface and morphological analyses

FE-SEM images of Ag_3VO_4 particles are presented in Fig. 6 and S9-14. It is noted that all samples present majority irregular particles and some regular morphologies particles in a high level of agglomeration/aggregation. In addition, there is wide range of the particle sizes, from tens of nanometers up to 1 μm.

The agglomeration and/or aggregation process, size heterogeneity, and the irregular particle morphologies are result of MAH methodology, which may have resulted random and uncontrolled growth between particles and a competitive process between nucleation and growth may have occurred [65–68]. The literature reports several synthesis methods to produce silver orthovanadate and its hybrid materials [95–97]. In view of these works, it is noted that the information obtained regarding the state of agglomeration and/or aggregation, size of particles, and their morphologies is in accordance with the literature and that changes in the synthesis parameters can provide significant variations in the size and morphologies of the particles obtained.

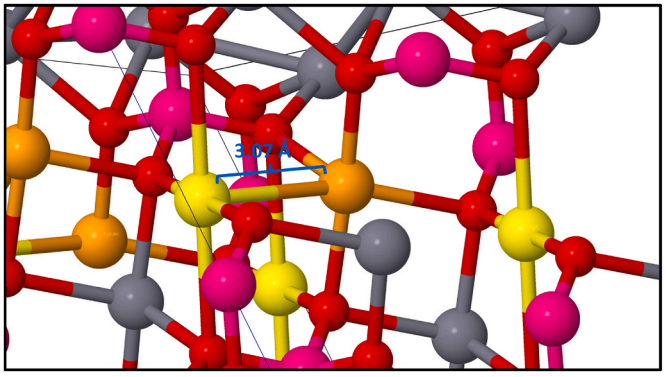

Fig. 5. Optimized structure of Ag_3VO_4 showing the location of interaction between the silver atoms in the structure. Vanadium, oxygen and silver atoms are represented by pink, red and gray colors, respectively. The interactive silvers are highlighted in yellow (Ag_P) and orange (Ag_S) colors. (For interpretation of the references to color in this figure legend, the reader is referred to the Web version of this article.)

Each crystalline structure presents several families of crystallographic planes, which represent different atomic packings or densities and, consequently, different energies [98,99]. Exposing different crystallographic planes may result in different surface energies [99]. Particle nucleation and growth are influenced by several variables, such as temperature, pressure, solvent, chemical species present in the system, pH, etc. [100]. The particle growth is finite, and during this process, according to the conditions of the system, certain surfaces are stimulated to their development, which may produce the relative decrease or extinction of other surfaces, and, in equilibrium, leads to the formation of more stable particle's morphologies [99]. This methodology includes microwaves irradiation, and it means that, according to the literature [101], there is a dissolution-recrystallization mechanism working on Ag_3VO_4 surface, whose synthesis time available and other experimental conditions were enough to provide changes on sample's morphology.

Moreover, in the literature, the possibility was reported for interaction between the electron beam produced by a scanning electron microscope and a silver-based semiconductor so that such interaction can provide different effects in the particles [102–107]. A common effect observed is the mass transfer of Ag atoms from the original particles to some preferential locations on the surface, where the nucleation and growth of nanometric metallic silver occurs [102,105,107]. Such interaction is possible to observe in Fig. 6 – 32b), 32c), 64b) and 64c). These images show *in situ* metallic silver growth on the surface. According to the literature, theoretical simulations show that the increase in electronic density in the conduction band promotes changes in the electronic structure [103–105,108]. In silver-based semiconductors, it is noted a tendency towards an increase in chemical bond length and, consequently, breaking Ag–O chemical bonds of clusters of the material by increasing the electronic density in the conduction band [103,104,108]. By breaking chemical bonds, the Ag^+ cation is reduced to Ag^0 and diffuses to energetically favorable surface regions to initiate the nucleation and growth processes of metallic silver [103,107]. The increase in electronic density also favors the process of atom diffusion through the reduction or even extinction of the energy barrier, which explains both the silver growth through silver atoms originating from the original material, and through the extinction or decrease of other metallic silver nuclei on the surface [103,107].

In order to get more details about morphology, Fig. 7 shows TEM images of the samples synthesized at 2 and 64 min. The images show particle size smaller than 50 nm and reveal partially nanometric character for samples, and agglomerated/aggregated particles. In FE-SEM images, irregular morphologies are noted for particles with a certain degree of spherical similarity and growth mechanism via orientated attachment, whose growth occurs by chemical bonding between two particles so that there are aligned crystallographic planes [100], as observed in Fig. 7 b).

In Fig. S7 are the EDS spectra of the samples synthesized for 2 and 64 min. O, Ag and V elements were detected, which correspond to those expected by the Ag_3VO_4 composition, and there is no indication of foreign impurities. Other peaks elements such as Cu, C and Si are attributed to the equipment and support grid.

The phase diagram depicted in Fig. 8 provides the information to investigate the (100), (010), (001), (101), (110), (011), and (111) surfaces stability, enabling the Wulff construction [109] for morphologies of Ag_3VO_4 nanoparticles, as a function of the Ag and O chemical potential. According to the Wulff construction, the crystal morphology depends on the surface energy of crystal planes, which can be

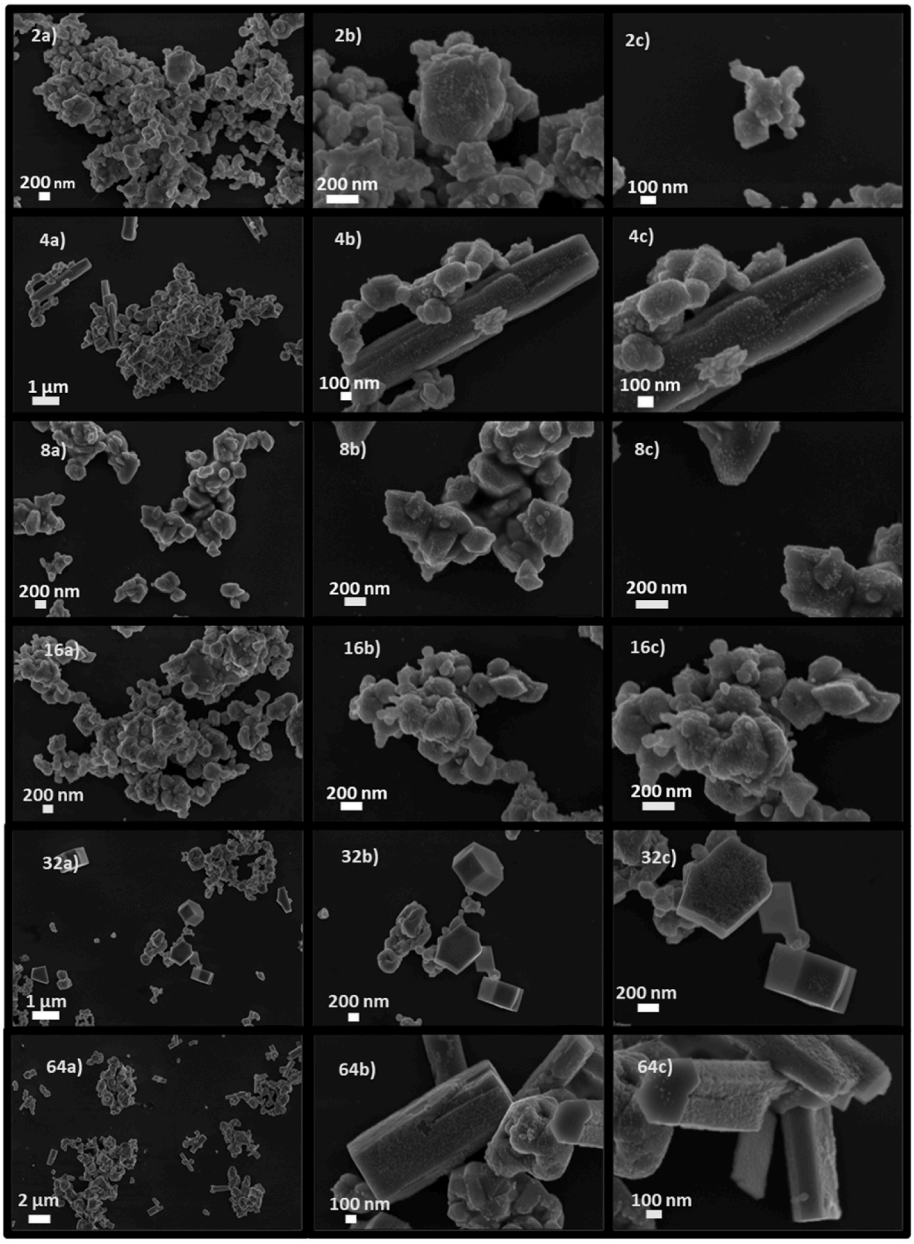

Fig. 6. FE-SEM images in different magnifications of the Ag_3VO_4 obtained by MAH method: 2a), 2b) and 2c) at 2 min; 4a), 4b) and 4c) at 4 min; 8a), 8b) and 8c) at 8 min; 16a), 16b) and 16c) at 16 min; 32a), 32b) and 32c) at 32 min; 64a), 64b) and 64c) at 64 min.

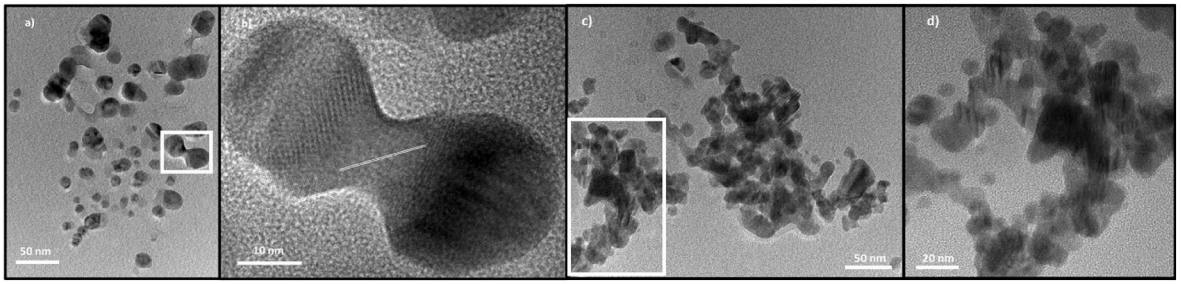

Fig. 7. Transmission electron microscopy images of Ag_3VO_4 obtained by MAH method in different magnifications: a) and b) in 2 min; c) and d) in 64 min.

interpreted as function of the chemical potentials of constituent atoms in a thermodynamic approach.

Firstly, due to the stability order of investigated surfaces, it was noted that (100) surface exhibits an extensive stabilization range, followed by (110), (101), and (111) surfaces. In particular, the A and B terminations of (100) surface exhibit a competition dependency upon the chemical potential. Moreover, considering the temperature values at different oxygen partial pressures (1 atm for normal experimental

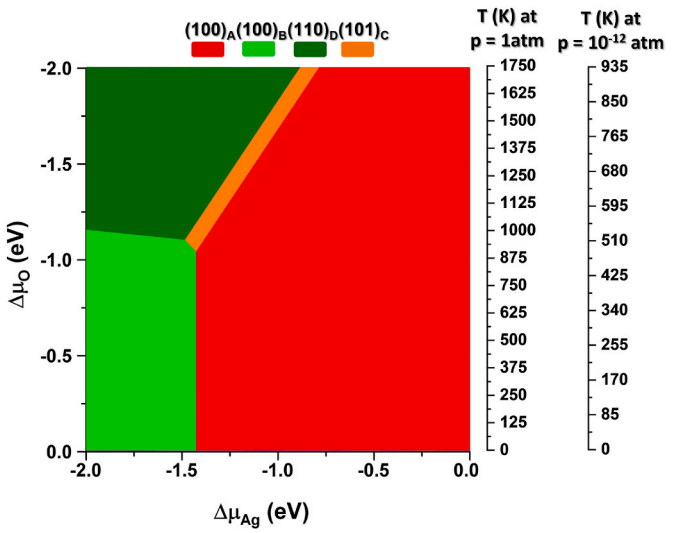

Fig. 8. Phase diagram of Ag_3VO_4 surfaces as a function of the oxygen and silver chemical potentials. Right panels is to convert values of oxygen chemical potential to easily observable values of temperature T at different oxygen partial pressure.

conditions and 10^{-12} atm for ultra-high vacuum (UHV)) it was observed that $(100)_A$ termination can be found at lower temperatures and more rich/poor O/Ag environment. On the other hand, $(100)_B$ termination can be found for higher temperatures at richer silver environments and extensive oxygen region. The $(110)_D$ surface is stable at higher temperatures (poor oxygen chemical potential region) and extensive silver region, while $(101)_C$ exhibits a small area in the phase diagram being associated with singular dependences with silver and oxygen environments. Focusing on the stability region of the building oxides (Ag_2O and V_2O_5), the phase diagram clearly indicates the higher stability of $(100)_A$ surface termination.

Furthermore, the Wulff construction was applied to obtain ideal shapes at different O/Ag chemical potentials, as presented in Fig. 9. It was observed that for silver rich ($\Delta\mu_{Ag} = 0.0$ eV) environment the

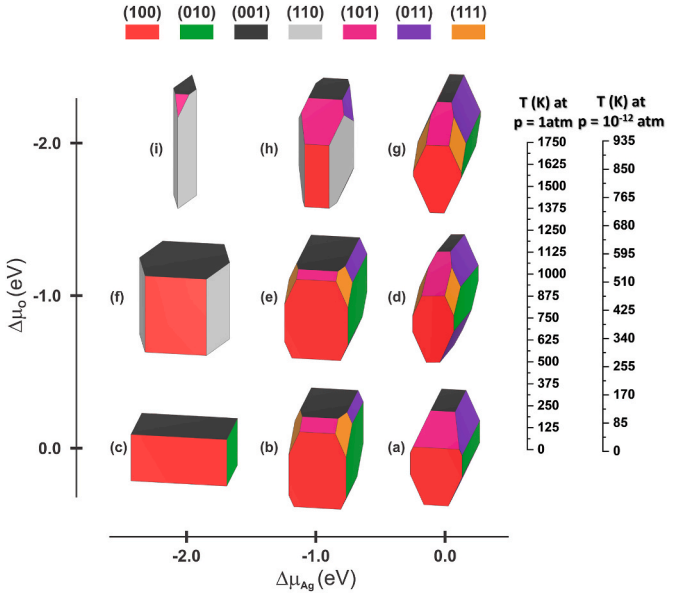

Fig. 9. Wulff morphologies obtained with the surface energy values as a function of oxygen and silver chemical potential. Right panels is to convert values of oxygen chemical potential to easily observable values of temperature T at different oxygen partial pressure.

obtained morphologies behave as octahedral shapes with corner and side-truncated habits depending upon the oxygen chemical potential (a, d, g). For the intermediate environment ($\Delta\mu_{Ag} = -1.0$ eV) the obtained morphologies can be described as corner-truncated cubic shapes (b, e) for richer oxygen environment and side/corner-truncated octahedral (h) polygon for oxygen-poor region. For silver-poor environment ($\Delta\mu_{Ag} = -2.0$ eV) more regular shapes were observed: (c) rectangular rod; (f) hexagonal rod; and (i) diamond-like rod. In this case, the morphological modulation is attributed to the decreasing of (110) and (101) surface energies values, moving the rectangular shape to diamond-like rod through a hexagonal morphology. The surface contribution to the overall polyhedron area was summarized in Table S8.

Comparing the obtained theoretical morphologies with the FE-SEM images, see Fig. 10, it was possible to ascertain that Ag_3VO_4 samples obtained at 4 and 64 min resemble the rectangular rod enclosing (100), (010) and (001) surfaces, while the sample obtained at 16, 32 and 64 min exhibit a hexagonal rod morphology enclosing (100), (001) and (110) surfaces, respectively. Moreover, the samples obtained at 4 and 6 min exhibit octahedral shapes with corner and side-truncated, that can be related to the theoretical morphology (a), (d) or (g) that encloses (100), (010), (001), (101), (011) and (111) surfaces. Moreover, the samples obtained at 64 min exhibit the same hexagonal cross-section morphology, but the MAH method induces some corner-truncations as well that can be related to the theoretical morphology (h) that encloses (100), (001), (110), (101) and (011) surfaces.

Finally, the thermodynamic pathways that describes the morphological modulations were investigated considering the polyhedron energy (E_{pol}) calculated as the combination between the surface energy values and the corresponding contribution to the polyhedron area, as presented in Table S8. Fig. 11 shows three different reaction paths for Ag_3VO_4. The morphological modulations in function of the oxygen chemical potential at $\Delta\mu_{Ag} = -2.0$ eV and $\Delta\mu_{Ag} = -1.0$ eV indicates an overall decreasing E_{pol} modulation, while the morphological pathway at rich silver ($\Delta\mu_{Ag} = 0.0$ eV) environment indicate an increasing E_{pol} modulation. These pathways can be understood comparing the surface energy values reported in Table S8. Moreover, based on the previous assumption that experimental morphological modulation associated with the synthesis time can be compared with the polyhedron modification at $\Delta\mu_{Ag} = -2.0$ eV, the obtained E_{pol} values indicate that the polyhedron energy may be reducted by generating elongated rod-like shapes. The major difference between the model is the surface orientation of the growing direction once the rectangular rod-like exhibits the (100) surface-orientation preference, (i) exhibits a larger (110) contribution, while the hexagonal shape exhibits a competition between (100)/(001)/(110) surfaces values indicates that the increasing synthesis time does not induce to modify polyhedron shapes, but it is possible to find different particle morphology at the same synthesis time.

Several studies were implemented in the literature making a bridge between experiments and theory involving morphological aspects of materials and their properties [110–113]. Surface has an important role in many applications, such as photocatalysis, bactericide activity, photoluminescent emissions and any other [110,112–114]. This simulation has shown as an important tool for understanding particles shape characteristics, such as surface energy provided by each surface and its contribution, which may help to better modulate surface shape produced for different synthesis method, and brings a greater property for a specific application.

4. Conclusions

Silver orthovanadate was synthesized by microwave-assisted hydrothermal method without the presence of secondary phases in short reactional times. The experimental results indicate synthesis time as a parameter was enough to slightly cause long-range order influence in the structure. MAH provided changes in long, medium and short-range order of the structure compared to different synthesis method reported

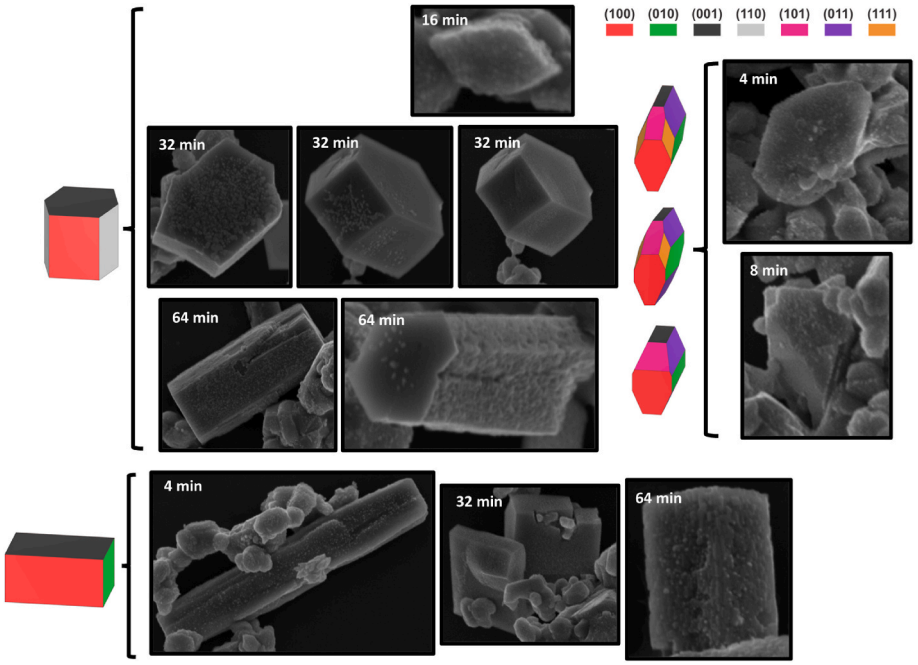

Fig. 10. Wulff morphologies associated to their correspondent experimental morphologies identified by FE-SEM for different time synthesis.

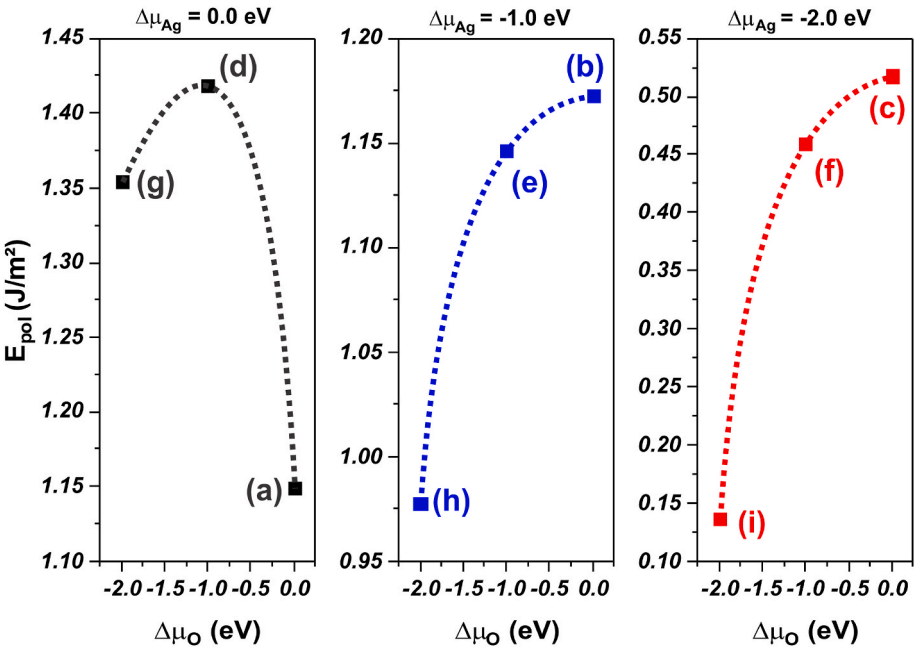

Fig. 11. Schematic illustration of the energy profile for different Ag_3VO_4 morphologies. The polyhedron energy, E_{pol}, is plotted versus the oxygen chemical potential. Intermediate morphologies were obtained by decreasing/increasing of E_{surf} values involved in the process.

in literature. Also, silver nanoparticle growth was observed on the silver orthovanadate's surface. The DFT calculations showed that part of this phenomenon may be explained by considering chemical interactions in the crystal structure. Also, there are silver cations interactions in this structure, and it may favor conditions to create silver nanoparticle seeds. All chemical interactions in silver orthovanadate structure are classified as transit. However, it was observed that the V–O chemical bonds present a degree of covalence superior to Ag–O chemical bonds. FE-SEM images showed that the MAH method was responsible for production of heterogeneous particle morphology, whose regular shapes were predicted by computational simulations. Finally, this study highlights the importance of theoretical and experimental understanding of silver orthovanadate structure for future applications.

CRediT authorship contribution statement

Guilherme Henrique Cruvinel: Conceptualization, Data curation, Formal analysis, Funding acquisition, Investigation, Methodology, Project administration, Resources, Software, Supervision, Validation, Visualization, Writing – original draft, Writing – review & editing. **Regiane Cristina de Oliveira:** Formal analysis, Investigation, Methodology, Writing – review & editing. **Marisa Carvalho de Oliveira:**

Data curation, Formal analysis, Investigation, Methodology, Software, Writing – original draft, Writing – review & editing. **Ivo Mateus Pinatti:** Formal analysis, Investigation, Methodology, Writing – original draft, Writing – review & editing. **Renan Augusto Pontes Ribeiro:** Data curation, Formal analysis, Funding acquisition, Investigation, Methodology, Software, Writing – original draft, Writing – review & editing. **Elson Longo:** Conceptualization, Data curation, Formal analysis, Funding acquisition, Investigation, Methodology, Project administration, Resources, Software, Supervision, Validation, Visualization, Writing – original draft, Writing – review & editing.

Declaration of competing interest

The authors declare that they have no known competing financial interests or personal relationships that could have appeared to influence the work reported in this paper.

Acknowledgments

The authors are grateful for the financial support of São Paulo Research Foundation (FAPESP; Grant #13/07296-2, 2020/11232-3, 2021/01651-1, 2022/16840-7 and 2021/11255-6), Coordenação de Aperfeiçoamento de Pessoal de Nível Superior-Brasil (CAPES) - Finance Code 001, Minas Gerais State Research Support Foundation (FAPEMIG. Grant No. APQ-00079-21), and UEMG for the Productivity Program. The authors are also grateful to the National Laboratory for Scientific Computing (LNCC) and the HighPerformance Computing Center (NACAD) at COPPE-UFRJ and to the National Center for High-Performance Computing (CENAPAD) at UNICAMP for providing computing resources.

Appendix A. Supplementary data

Supplementary data to this article can be found online at https://doi.org/10.1016/j.ceramint.2024.05.252.

References

[1] H. Duan, D. Wang, Y. Li, Green chemistry for nanoparticle synthesis, Chem. Soc. Rev. 44 (2015) 5778–5792, https://doi.org/10.1039/C4CS00363B.
[2] H.J. Kitchen, S.R. Vallance, J.L. Kennedy, N. Tapia-Ruiz, L. Carassiti, A. Harrison, A.G. Whittaker, T.D. Drysdale, S.W. Kingman, D.H. Gregory, Modern microwave methods in solid-state inorganic materials chemistry: from fundamentals to manufacturing, Chem. Rev. 114 (2014) 1170–1206, https://doi.org/10.1021/cr4002353.
[3] J. Pawliszyn, J.M. Bayona, P. Dugo, X.C. Le, H.K. Lee, X.-F. Li, H. Lord (Eds.), Comprehensive Sampling and Sample Preparation: Analytical Techniques for Scientists, first ed., Academic Press, Amsterdam, 2012.
[4] M.B. Gawande, S.N. Shelke, R. Zboril, R.S. Varma, Microwave-assisted chemistry: synthetic applications for rapid assembly of nanomaterials and organics, Acc. Chem. Res. 47 (2014) 1338–1348, https://doi.org/10.1021/ar400309b.
[5] S. Horikoshi, N. Serpone, Microwaves in Nanoparticle Synthesis: Fundamentals and Applications, first ed., Wiley-VCH Verlag GmbH, Baden, 2013.
[6] S.V. Kumar, A.P. Bafana, P. Pawar, A. Rahman, S.A. Dahoumane, C.S. Jeffryes, High conversion synthesis of <10 Nm starch-stabilized silver nanoparticles using microwave technology, Sci. Rep. 8 (2018) 5106, https://doi.org/10.1038/s41598-018-23480-6.
[7] V.R. Mendonça, O.F. Lopes, W. Avansi, R. Arenal, C. Ribeiro, Insights into formation of anatase TiO2 nanoparticles from peroxo titanium complex degradation under microwave-assisted hydrothermal treatment, Ceram. Int. 45 (2019) 22998–23006, https://doi.org/10.1016/j.ceramint.2019.07.345.
[8] M.B. Mohamed, K.M. AbouZeid, V. Abdelsayed, A.A. Aljarash, M.S. El-Shall, Growth mechanism of anisotropic gold nanocrystals via microwave synthesis: formation of dioleamide by gold nanocatalysis, ACS Nano 4 (2010) 2766–2772, https://doi.org/10.1021/nn9016179.
[9] S. de C. Pereira, A.T. de Figueiredo, C.M. Barrado, M.H. Stoppa, T.O. dos Santos, F.M. Pontes, E. Longo, Fast and efficient microwave-assisted synthesis of CaTiO3, Mater. Res. Express 4 (2017) 065014, https://doi.org/10.1088/2053-1591/aa7483.
[10] Y.-J. Zhu, F. Chen, Microwave-assisted preparation of inorganic nanostructures in liquid phase, Chem. Rev. 114 (2014) 6462–6555, https://doi.org/10.1021/cr400366s.
[11] F.J.S. Barros, K.L.P. Cardozo, G.H. Cruvinel, E. Longo, M.A.S. Garcia, A. A. Tanaka, I.M. Pinatti, Microwave-assisted hydrothermal synthesis of CeVO4 nanostructures: exploring their applicability in supercapacitor technologies, J. Mater. Sci. 59 (2024) 4236–4251, https://doi.org/10.1007/s10853-024-09487-7.
[12] M.M. Teixeira, I.M. Pinatti, J.A.S. Laranjeira, G.S.L. Fabris, M.D. Teodoro, I.L. V. Rosa, A.Z. Simões, J. Andrés, J.R. Sambrano, E. Longo, Photoluminescence of Ca10V6O25:Eu3+: a theoretical and experimental approach, J. Alloys Compd. 980 (2024) 173525, https://doi.org/10.1016/j.jallcom.2024.173525.
[13] F.J.S. Barros, K.L.P. Cardoso, E. Longo, A.A. Tanaka, M.A.S. Garcia, I.M. Pinatti, Facile microwave-assisted hydrothermal synthesis of GdVO4 nanospheres: unlocking their potential as electrodes for supercapacitors, J. Mater. Sci. 58 (2023) 15459–15470, https://doi.org/10.1007/s10853-023-08984-5.
[14] A. ChauhanSonu, P. Raizada, P. Singh, T. Ahamad, V.-H. Nguyen, Q. Van Le, A. Aslam Parwaz Khan, N. Kumar, A. Sudhaik, C. Mustansar Hussain, A recent developments in Ag3VO4 based photocatalysts towards environmental remediation: properties, synthesis, strategies and applications, J. Ind. Eng. Chem. 130 (2024) 25–53, https://doi.org/10.1016/j.jiec.2023.09.042.
[15] B. Zhai, Y. Chen, Y. Liang, Y. Gao, J. Shi, H. Zhang, Y. Li, Modifying Ag3VO4 with metal-organic frameworks for enhanced photocatalytic activity under visible light, Mater. Chem. Phys. 239 (2020) 122078, https://doi.org/10.1016/j.matchemphys.2019.122078.
[16] W. Wei, S. Yang, F. Guo, J. Lu, Z. Jiang, Decoration of monodisperse silver vanadate on biomass-derived porous carbon: a dual-purpose catalyst for detection of p-nitrophenol and photodegradation of rhodamine B, Adv. Energy Sustain. Res. 4 (2023) 2370014, https://doi.org/10.1002/aesr.202370014.
[17] D. Leng, R. Xu, L. Liu, H. Wang, J. Li, X. Ren, Q. Wei, H. Ju, Rationally engineered high-performance BiVO4/Ag3VO4/SnS2 photoelectrodes for ultrasensitive immunosensing of CYFRA21-1 based on HRP-tyramine-triggered insoluble precipitates, Microchim. Acta 188 (2021) 270, https://doi.org/10.1007/s00604-021-04938-3.
[18] S. Kumaran, K.G. Revathi, R. Dayana, S. Maheswari, Enhancing the photocatalytic activity of a TiO2/Ag3VO4 hybrid composite for optoelectronic and solar energy conversion applications, J. Electron. Mater. 53 (2024) 1989–2002, https://doi.org/10.1007/s11664-024-10939-8.
[19] A. Fujishima, K. Honda, Electrochemical photolysis of water at a semiconductor electrode, Nature 238 (1972) 37–38, https://doi.org/10.1038/238037a0.
[20] R. Georgekutty, M.K. Seery, S.C. Pillai, A highly efficient Ag-ZnO photocatalyst: synthesis, properties, and mechanism, J. Phys. Chem. C 112 (2008) 13563–13570, https://doi.org/10.1021/jp802729a.
[21] X. Zhang, B. Gao, R. Rao, F. Bi, C. Li, K. Yue, Y. Wang, J. Xu, X. Feng, Y. Yang, Defects materials of Institut Lavoisier-125(Ti) materials enhanced photocatalytic activity for toluene and chlorobenzene mixtures degradation: mechanism study, J. Colloid Interface Sci. 660 (2024) 423–439, https://doi.org/10.1016/j.jcis.2024.01.012.
[22] J. Chen, Y. Yang, S. Zhao, F. Bi, L. Song, N. Liu, J. Xu, Y. Wang, X. Zhang, Stable black phosphorus encapsulation in porous mesh-like UiO-66 promoted charge transfer for photocatalytic oxidation of toluene and o-dichlorobenzene: performance, degradation pathway, and mechanism, ACS Catal. 12 (2022) 8069–8081, https://doi.org/10.1021/acscatal.2c01375.
[23] X. Zhang, K. Yue, R. Rao, J. Chen, Q. Liu, Y. Yang, F. Bi, Y. Wang, J. Xu, N. Liu, Synthesis of acidic MIL-125 from plastic waste: significant contribution of N orbital for efficient photocatalytic degradation of chlorobenzene and toluene, Appl. Catal. B Environ. 310 (2022) 121300, https://doi.org/10.1016/j.apcatb.2022.121300.
[24] F. Bi, S. Ma, B. Gao, Y. Yang, L. Wang, F. Fei, J. Xu, Y. Huang, M. Wu, X. Zhang, Non-oxide supported Pt-metal-group catalysts for efficiently CO and toluene co-oxidation: difference in water resistance and degradation intermediates, Fuel 344 (2023) 128147, https://doi.org/10.1016/j.fuel.2023.128147.
[25] X. Zhang, R. Rao, B. Gao, S. Ma, F. Bi, C. Li, Z. Zhu, N. Liu, Y. Yang, Z. Wang, Crystal engineering of TiO2 enhanced photothermal catalytic degradation of DEHP on Pt catalysts, Mater. Today Chem. 34 (2023) 101755, https://doi.org/10.1016/j.mtchem.2023.101755.
[26] Y. Yang, S. Zhao, F. Bi, J. Chen, Y. Li, L. Cui, J. Xu, X. Zhang, Oxygen-vacancy-induced O2 activation and electron-hole migration enhance photothermal catalytic toluene oxidation, Cell Rep. Phys. Sci. 3 (2022) 101011, https://doi.org/10.1016/j.xcrp.2022.101011.
[27] Sh Deylami, M.H. Sabzevari, M. Ghaedi, M.H.A. Azqhandi, F. Marahel, Efficient photodegradation of disulfine blue dye and Tetracycline over Robust and Green g-CN/Ag3VO4/PAN nanofibers: experimental design, RSM, RBF-NN and ANFIS modeling, Process Saf. Environ. Protect. 169 (2023) 71–81, https://doi.org/10.1016/j.psep.2022.10.080.
[28] J. Chen, H. Zhu, Q. Ren, S. Chen, Y. Ding, Z. Jin, C. Xiong, W. Guo, X. Jia, Efficient degradation of atrazine residues in wastewater by persulfate assisted Ag3VO4/Bi2MoO6/diatomite under visible light, J. Environ. Chem. Eng. 10 (2022) 107938, https://doi.org/10.1016/j.jece.2022.107938.
[29] A. Vali, P.S. Toth, H.-W. Jee, F. Firouzan, C. Janáky, K.-J. Paeng, N. Myung, K. Rajeshwar, Electrosynthesis and properties of crystalline and phase-pure silver orthovanadate, J. Phys. Chem. C 124 (2020) 19980–19989, https://doi.org/10.1021/acs.jpcc.0c05421.
[30] S. Li, S. Hu, W. Jiang, Y. Liu, J. Liu, Z. Wang, Facile synthesis of flower-like Ag3VO4/Bi2WO6 heterojunction with enhanced visible-light photocatalytic activity, J. Colloid Interface Sci. 501 (2017) 156–163, https://doi.org/10.1016/j.jcis.2017.04.057.
[31] V. Cloet, A. Raw, K.R. Poeppelmeier, G. Trimarchi, H. Peng, J. Im, A.J. Freeman, N.H. Perry, T.O. Mason, A. Zakutayev, P.F. Ndione, D.S. Ginley, J.D. Perkins, Structural, optical, and transport properties of α- and β-Ag3VO4, Chem. Mater. 24 (2012) 3346–3354, https://doi.org/10.1021/cm301119c.

[32] T.A. Albrecht, C.L. Stern, K.R. Poeppelmeier, The Ag2O-V2O5-HF((aq)) system and crystal structure of alpha-Ag3VO4, Inorg. Chem. 46 (2007) 1704–1708, https://doi.org/10.1021/ic062138+.
[33] G. Trimarchi, H. Peng, J. Im, A.J. Freeman, V. Cloet, A. Raw, K.R. Poeppelmeier, K. Biswas, S. Lany, A. Zunger, Using design principles to systematically plan the synthesis of hole-conducting transparent oxides: Cu3VO4 and Ag3VO4 as a case study, Phys. Rev. B 84 (2011) 165116, https://doi.org/10.1103/PhysRevB.84.165116.
[34] W.D. Kingery, H.K. Bowen, D.R. Uhlmann, Introduction to Ceramics, second ed., John Wiley & Sons, New York, 1976.
[35] G.-T. Pan, M.-H. Lai, R.-C. Juang, T.-W. Chung, T.C.-K. Yang, Preparation of visible-light-driven silver vanadates by a microwave-assisted hydrothermal method for the photodegradation of volatile organic vapors, Ind. Eng. Chem. Res. 50 (2011) 2807–2814, https://doi.org/10.1021/ie1012932.
[36] X.H. Liao, Y. Liu, Z.H. Xu, X.D. Chen, R. Wang, The microwave synthesis and photocatalytic activity of silver vanadate, Adv. Mater. Res. 560–561 (2012) 191–201. https://doi.org/10.4028/www.scientific.net/AMR.560-561.191.
[37] N.F.A. Neto, T.B.O. Nunes, M. Li, E. Longo, M.R.D. Bomio, F.V. Motta, Influence of microwave-assisted hydrothermal treatment time on the crystallinity, morphology and optical properties of ZnWO4 nanoparticles: photocatalytic activity, Ceram. Int. 46 (2020) 1766–1774, https://doi.org/10.1016/j.ceramint.2019.09.151.
[38] F.K.F. Oliveira, A.A.G. Santiago, A.C. Catto, L.F. da Silva, R.L. Tranquilin, E. Longo, F.V. Motta, M.R.D. Bomio, Cerium molybdate nanocrystals: microstructural, optical and gas-sensing properties, J. Alloys Compd. 857 (2021) 157562, https://doi.org/10.1016/j.jallcom.2020.157562.
[39] R.C. Oliveira, M.M. Teixeira, J.P.C. Costa, M. Penha, E.M. Francisco, J.S. da Silva, M.S. Li, E. Longo, L. Gracia, J. Andrés, α- and β-AgVO3 polymorphs as photoluminescent materials: an example of temperature-driven synthesis, Ceram. Int. 44 (2018) 5939–5944, https://doi.org/10.1016/j.ceramint.2017.12.161.
[40] H.T.S. Britton, R.A. Robinson, Physicochemical studies of complex acids. Part IV. The vanadates of silver, J. Chem. Soc. 0 (1930) 2328–2343, https://doi.org/10.1039/JR9300002328.
[41] D.R. Lide, CRC Handbook of Chemistry and Physics, eighty-fourth ed., CRC Press, Boca Raton, FL, 2003.
[42] A. Seidell, W.F. Linke, Solubilities of Inorganic and Organic Compounds a Compilation of Quantitative Solubility Data from the Periodical Literature, third ed., Van Nostrand, 1952.
[43] R.E. Dinnebier, A. Kowalevsky, H. Reichert, M. Jansen, Polymorphism of Ag3VO4, Z. Kristallogr. 222 (2007) 420–426, https://doi.org/10.1524/zkri.2007.222.8.420.
[44] B.H. Toby, R.B. Von Dreele, GSAS-II: the genesis of a modern open-source all purpose crystallography software package, J. Appl. Crystallogr. 46 (2013) 544–549, https://doi.org/10.1107/S0021889813003531.
[45] A.D. Becke, Density-functional exchange-energy approximation with correct asymptotic behavior, Phys. Rev. A 38 (1988) 3098–3100, https://doi.org/10.1103/PhysRevA.38.3098.
[46] C. Lee, W. Yang, R.G. Parr, Development of the colle-salvetti correlation-energy formula into a functional of the electron density, Phys. Rev. B Condens. Matter 37 (1988) 785–789, https://doi.org/10.1103/physrevb.37.785.
[47] S. Grimme, J. Antony, S. Ehrlich, H. Krieg, A consistent and accurate ab initio parametrization of density functional dispersion correction (DFT-D) for the 94 elements H-Pu, J. Chem. Phys. 132 (2010) 154104, https://doi.org/10.1063/1.3382344.
[48] R. Dovesi, A. Erba, R. Orlando, C.M. Zicovich-Wilson, B. Civalleri, L. Maschio, M. Rérat, S. Casassa, J. Baima, S. Salustro, B. Kirtman, Quantum-mechanical condensed matter simulations with CRYSTAL, WIREs Comput. Mol. Sci. 8 (2018) e1360, https://doi.org/10.1002/wcms.1360.
[49] T. Bredow, K. Jug, R.A. Evarestov, Electronic and magnetic structure of ScMnO3, Phys. Status Solidi B 243 (2006) R10–R12, https://doi.org/10.1002/pssb.200541403.
[50] E. Aprà, E. Stefanovich, R. Dovesi, C. Roetti, An ab initio hartree—fock study of silver chloride, Chem. Phys. Lett. 186 (1991) 329–335, https://doi.org/10.1016/0009-2614(91)90187-E.
[51] W.C. Mackrodt, N.M. Harrison, V.R. Saunders, N.L. Allan, M.D. Towler, E. Aprà, R. Dovesi, Ab initio Hartree-Fock calculations of CaO, VO, MnO and NiO, Philos. Mag. A 68 (1993) 653–666, https://doi.org/10.1080/01418619308213989.
[52] H.J. Monkhorst, J.D. Pack, Special points for brillouin-zone integrations, Phys. Rev. B 13 (1976) 5188–5192, https://doi.org/10.1103/PhysRevB.13.5188.
[53] L. Maschio, B. Kirtman, M. Rérat, R. Orlando, R. Dovesi, Ab initio analytical Raman intensities for periodic systems through a coupled perturbed Hartree-Fock/Kohn-Sham method in an atomic orbital basis. II. Validation and comparison with experiments, J. Chem. Phys. 139 (2013) 164102, https://doi.org/10.1063/1.4824443.
[54] F. Pascale, C.M. Zicovich-Wilson, F. López Gejo, B. Civalleri, R. Orlando, R. Dovesi, The calculation of the vibrational frequencies of crystalline compounds and its implementation in the CRYSTAL code, J. Comput. Chem. 25 (2004) 888–897, https://doi.org/10.1002/jcc.20019.
[55] C.M. Zicovich-Wilson, F. Pascale, C. Roetti, V.R. Saunders, R. Orlando, R. Dovesi, Calculation of the vibration frequencies of alpha-quartz: the effect of Hamiltonian and basis set, J. Comput. Chem. 25 (2004) 1873–1881, https://doi.org/10.1002/jcc.20120.
[56] C. Gatti, S. Casassa, TOPOND14 user's manual, CNR-ISTM of milano, milano. https://www.crystal.unito.it/topond/topond.pdf, 2017. (Accessed 14 December 2023).
[57] R.F.W. Bader, Atoms in Molecules: A Quantum Theory, Oxford University Press, Oxford, 1990.
[58] K. Reuter, M. Scheffler, Composition, structure, and stability of RuO2(110) as a function of oxygen pressure, Phys. Rev. B 65 (2001) 035406, https://doi.org/10.1103/PhysRevB.65.035406.
[59] J.C. Moreno-Pirajan, Thermodynamics - Interaction Studies - Solids, Liquids and Gases, InTech, 2011, https://doi.org/10.5772/823.
[60] P. Linstrom, W.G. Mallard, NIST Chemistry WebBook, NIST Standard Reference Database Number 69, National Institute of Standards and Technology, Gaithersburg MD, 2017. https://webbook.nist.gov/chemistry/. (Accessed 25 November 2023).
[61] R.A.P. Ribeiro, M.C. Oliveira, M.R.D. Bomio, S.R. de Lazaro, J. Andrés, E. Longo, Connecting the surface structure, morphology and photocatalytic activity of Ag2O: an in depth and unified theoretical investigation, Appl. Surf. Sci. 509 (2020) 145321, https://doi.org/10.1016/j.apsusc.2020.145321.
[62] V. Jagadeesha Angadi, K. Manjunatha, M.C. Oliveira, E. Longo, S.R. de Lázaro, R. A.P. Ribeiro, S.V. Bhat, Unveiling the shape-selective CoCr2-yScyO4 nanomagnetism, Appl. Surf. Sci. 574 (2022) 151555, https://doi.org/10.1016/j.apsusc.2021.151555.
[63] K. Manjunatha, V.J. Angadi, M.C. Oliveira, S.R. de Lazaro, E. Longo, R.a. P. Ribeiro, S.O. Manjunatha, N.H. Ayachit, Towards shape-oriented Bi-doped CoCr2O4 nanoparticles from theoretical and experimental perspectives: structural, morphological, optical, electrical and magnetic properties, J. Mater. Chem. C 9 (2021) 6452–6469, https://doi.org/10.1039/D1TC00872B.
[64] K. Momma, F. Izumi, VESTA 3 for three-dimensional visualization of crystal, volumetric and morphology data, J. Appl. Crystallogr. 44 (2011) 1272–1276, https://doi.org/10.1107/S0021889811038970.
[65] M. Hosokawa, M. Naito, K. Nogi, T. Yokoyama (Eds.), Nanoparticle Technology Handbook, first ed., Elsevier, 2007.
[66] Y. Kim, U. Platt, M.B. Gu, H. Iwahashi (Eds.), Atmospheric and Biological Environmental Monitoring, Springer, Berlin, 2009.
[67] B.K. Park, S. Jeong, D. Kim, J. Moon, S. Lim, J.S. Kim, Synthesis and size control of monodisperse copper nanoparticles by polyol method, J. Colloid Interface Sci. 311 (2007) 417–424, https://doi.org/10.1016/j.jcis.2007.03.039.
[68] L.L. Schramm, Dictionary of nanotechnology. Colloid and Interface Science, first ed., Wiley-VCH, Weinheim, 2008.
[69] J. Lu, Handbook of measurement of residual stresses, Society for Experimental Mechanics, GA (1996).
[70] R.C. Oliveira, M. Assis, M.M. Teixeira, M.D.P. Silva, M.S. Li, J. Andres, L. Gracia, E. Longo, An experimental and computational study of β-AgVO3: optical properties and formation of Ag nanoparticles, J. Phys. Chem. C 120 (2016) 12254–12264, https://doi.org/10.1021/acs.jpcc.6b02840.
[71] N.N. Hoang, D.H.Y. Pham, T.N. Nguyen, Strain-Dependent structure and Raman behaviours in the heavy-ion irradiated manganite at extreme low dose, Sci. Rep. 9 (2019) 19204, https://doi.org/10.1038/s41598-019-55638-1.
[72] M.V. Kharlamova, Raman spectroscopy study of the doping effect of the encapsulated iron, cobalt, and nickel bromides on single-walled carbon nanotubes, J. Spectrosc. 2015 (2015) e653848, https://doi.org/10.1155/2015/653848.
[73] S. Mignuzzi, A.J. Pollard, N. Bonini, B. Brennan, I.S. Gilmore, M.A. Pimenta, D. Richards, D. Roy, Effect of disorder on Raman scattering of single-layer MoS2, Phys. Rev. B 91 (2015) 195411, https://doi.org/10.1103/PhysRevB.91.195411.
[74] Z.I. Zaki, M.S. Amin, R.M. Mohamed, I.A. Mkhalid, Sol–gel assembled Ag3VO4/rGO nanocomposite photocatalyst for improved visible-light-photooxidative desulfurization of thiophene, J. Inorg. Organomet. Polym. Mater. 31 (2021) 2999–3010, https://doi.org/10.1007/s10904-021-01895-5.
[75] S.M. Aouadi, D.P. Singh, D.S. Stone, K. Polychronopoulou, F. Nahif, C. Rebholz, C. Muratore, A.A. Voevodin, Adaptive VN/Ag nanocomposite coatings with lubricious behavior from 25 to 1000 °C, Acta Mater. 58 (2010) 5326–5331, https://doi.org/10.1016/j.actamat.2010.06.006.
[76] R.C. Oliveira, C.C. Foggi, M.M. Teixeira, M.D.P. Silva, M. Assis, E.M. Francisco, S. Pimentel, S. Pereira, C.E. Vergani, A.L. Machado, J. Andres, L. Gracia, E. Longo, Mechanism of antibacterial activity via morphology change of α-AgVO3: theoretical and experimental insights, ACS Appl. Mater. Interfaces 9 (2017) 11472–11481, https://doi.org/10.1021/acsami.7b00920.
[77] X. Kong, Z. Guo, C. Zeng, J. Huang, L. Cao, L. Li, L. Yin, P. Wen, Q. Feng, Z. Xu, Soft chemical in situ synthesis, formation mechanism and electrochemical performances of 1D bead-like AgVO3 nanoarchitectures, J. Mater. Chem. A 3 (2015) 18127–18135, https://doi.org/10.1039/C5TA05110J.
[78] R.L. Frost, K.L. Erickson, M.L. Weier, O. Carmody, Raman and infrared spectroscopy of selected vanadates, Spectrochim. Acta. A. Mol. Biomol. Spectrosc. 61 (2005) 829–834, https://doi.org/10.1016/j.saa.2004.06.006.
[79] S.-J. Bao, Q.-L. Bao, C.-M. Li, T.P. Chen, C.-Q. Sun, Z.-L. Dong, Y. Gan, J. Zhang, Synthesis and electrical transport of novel channel-structured beta-AgVO3, Small Weinh. Bergstr. Ger. 3 (2007) 1174–1177, https://doi.org/10.1002/smll.200700032.
[80] W. Zhao, Y. Guo, S. Wang, H. He, C. Sun, S. Yang, A novel ternary plasmonic photocatalyst: ultrathin g-C3N4 nanosheet hybrided by Ag/AgVO3 nanoribbons with enhanced visible-light photocatalytic performance, Appl. Catal. B Environ. 165 (2015) 335–343, https://doi.org/10.1016/j.apcatb.2014.10.016.
[81] J.-M. Song, Y.-Z. Lin, H.-B. Yao, F.-J. Fan, X.-G. Li, S.-H. Yu, Superlong β-AgVO3 nanoribbons: high-yield synthesis by a pyridine-assisted solution approach, their stability, electrical and electrochemical properties, ACS Nano 3 (2009) 653–660, https://doi.org/10.1021/nn800813s.
[82] S. Chandramohan, A. Kanjilal, J.K. Tripathi, S.N. Sarangi, R. Sathyamoorthy, T. Som, Structural and optical properties of Mn-doped CdS thin films prepared by

ion implantation, J. Appl. Phys. 105 (2009) 123507, https://doi.org/10.1063/1.3151712.
[83] A.L.B. Baccaro, I.G.R. Gutz, Fotoeletrocatálise Em Semicondutores: Dos Princípios Básicos Até Sua Conformação à Nanoescala, Quím. Nova 41 (2018) 326–339, https://doi.org/10.21577/0100-4042.20170174.
[84] W.D. Chemelewski, O. Mabayoje, C.B. Mullins, SILAR growth of Ag3VO4 and characterization for photoelectrochemical water oxidation, J. Phys. Chem. C 119 (2015) 26803–26808, https://doi.org/10.1021/acs.jpcc.5b06658.
[85] L. Zhang, Y. He, P. Ye, W. Qin, Y. Wu, T. Wu, Enhanced photodegradation activity of rhodamine B by Co3O4/Ag3VO4 under visible light irriadiation, Mater. Sci. Eng. B 178 (2013) 45–52, https://doi.org/10.1016/j.mseb.2012.10.011.
[86] L. Gao, Z. Li, J. Liu, Facile synthesis of Ag3VO4/β-AgVO3 nanowires with efficient visible-light photocatalytic activity, RSC Adv. 7 (2017) 27515–27521, https://doi.org/10.1039/C7RA03955G.
[87] F. Kiantazh, A. Habibi-Yangjeh, Ag3VO4/ZnO nanocomposites with an n– n heterojunction as novel visible-light-driven photocatalysts with highly enhanced activity, Mater. Sci. Semicond. Process. 39 (2015) 671–679, https://doi.org/10.1016/j.mssp.2015.06.011.
[88] D. Roy, G.F. Samu, M.K. Hossain, C. Janáky, K. Rajeshwar, On the measured optical bandgap values of inorganic oxide semiconductors for solar fuels generation, Catal. Today 300 (2018) 136–144, https://doi.org/10.1016/j.cattod.2017.03.016.
[89] C. Peng, Y. Liu, J. Cui, K. Luo, Y. Shen, X. Li, First-principle calculation of the electronic structure of α-Ag3VO4 using two different exchange correlation functionals, Mater. Chem. Phys. 262 (2021) 124307, https://doi.org/10.1016/j.matchemphys.2021.124307.
[90] C. Gatti, Chemical bonding in crystals: new directions, Z. Für Krist. - Cryst. Mater. 220 (2005) 399–457, https://doi.org/10.1524/zkri.220.5.399.65073.
[91] Y.V. Nelyubina, M.Y. Antipin, K.A. Lyssenko, Anion–anion interactions: their nature, energy and role in crystal formation, Russ. Chem. Rev. 79 (2010) 167, https://doi.org/10.1070/RC2010v079n03ABEH004120.
[92] D.V. Korabel'nikov, Y.N. Zhuravlev, The nature of the chemical bond in oxyanionic crystals based on QTAIM topological analysis of electron densities, RSC Adv. 9 (2019) 12020–12033, https://doi.org/10.1039/C9RA01403A.
[93] A.M. Pendás, A. Costales, V. Luaña, Ions in crystals: the topology of the electron density in ionic materials. III. Geometry and ionic radii, J. Phys. Chem. B 102 (1998) 6937–6948, https://doi.org/10.1021/jp980906f.
[94] D. Braga, F. Grepioni, J.J. Novoa, Inter-anion O–H–···O– hydrogen bond like interactions: the breakdown of the strength–length analogy, Chem. Commun. (1998) 1959–1960, https://doi.org/10.1039/A804392B.
[95] S. Wang, D. Li, C. Sun, S. Yang, Y. Guan, H. He, Synthesis and characterization of G-C3N4/Ag3VO4 composites with significantly enhanced visible-light photocatalytic activity for triphenylmethane dye degradation, Appl. Catal. B Environ. 144 (2014) 885–892, https://doi.org/10.1016/j.apcatb.2013.08.008.
[96] V.R. Raja, D.R. Rosaline, A. Suganthi, M. Rajarajan, Ultrasonic assisted synthesis with enhanced visible-light photocatalytic activity of NiO/Ag3VO4 nanocomposite and its antibacterial activity, Ultrason. Sonochem. 44 (2018) 73–85, https://doi.org/10.1016/j.ultsonch.2018.02.010.
[97] H.E. Emam, H.B. Ahmed, E. Gomaa, M.H. Helal, R.M. Abdelhameed, Doping of silver vanadate and silver tungstate nanoparticles for enhancement the photocatalytic activity of MIL-125-NH2 in dye degradation, J. Photochem. Photobiol. Chem. 383 (2019) 111986, https://doi.org/10.1016/j.jphotochem.2019.111986.
[98] W.D. Callister Jr., Materials Science and Engineering: an Introduction, seventh ed., John Wiley & Sons, New York, 2007.
[99] A.F. Gouveia, L. Gracia, E. Longo, M.A. San-Miguel, J. Andrés, Modulating the properties of multifunctional semiconductors by means of morphology: theory meets experiments, Comput. Mater. Sci. 188 (2021) 110217.
[100] N.T.K. Thanh, N. Maclean, S. Mahiddine, Mechanisms of nucleation and growth of nanoparticles in solution, Chem. Rev. 114 (2014) 7610–7630, https://doi.org/10.1021/cr400544s.
[101] Y.B. Khollam, A.S. Deshpande, A.J. Patil, H.S. Potdar, S.B. Deshpande, S.K. Date, Microwave-hydrothermal synthesis of equi-axed and submicron-sized BaTiO3 powders, Mater. Chem. Phys. 71 (2001) 304–308, https://doi.org/10.1016/S0254-0584(01)00286-3.
[102] M. Assis, T. Robeldo, C.C. Foggi, A.M. Kubo, G. Mínguez-Vega, E. Condoncillo, H. Beltran-Mir, R. Torres-Mendieta, J. Andrés, M. Oliva, C.E. Vergani, P. A. Barbugli, E.R. Camargo, R.C. Borra, E. Longo, Ag nanoparticles/α-Ag 2 WO 4 composite formed by electron beam and femtosecond irradiation as potent antifungal and antitumor agents, Sci. Rep. 9 (2019) 9927, https://doi.org/10.1038/s41598-019-46159-y.
[103] J. Andres, A.F. Gouveia, L. Gracia, E. Longo, G.M. Faccin, E.Z. da Silva, D. H. Pereira, M.A. San-Miguel, Formation of Ag nanoparticles under electron beam irradiation: atomistic origins from first-principles calculations, Int. J. Quant. Chem. 118 (2018) e25551, https://doi.org/10.1002/qua.25551.
[104] M.T. Fabbro, L. Gracia, G.S. Silva, L.P.S. Santos, J. Andrés, E. Cordoncillo, E. Longo, Understanding the formation and growth of Ag nanoparticles on silver chromate induced by electron irradiation in electron microscope: a combined experimental and theoretical study, J. Solid State Chem. 239 (2016) 220–227, https://doi.org/10.1016/j.jssc.2016.03.050.
[105] E. Longo, L.S. Cavalcante, D.P. Volanti, A.F. Gouveia, V.M. Longo, J.A. Varela, M. O. Orlandi, J. Andrés, Direct in situ observation of the electron-driven synthesis of Ag filaments on α-Ag 2 WO 4 crystals, Sci. Rep. 3 (2013) 1676, https://doi.org/10.1038/srep01676.
[106] M.A. San-Miguel, E.Z. da Silva, S.M. Zanetti, M. Cilense, M.T. Fabbro, L. Gracia, J. Andrés, E. Longo, In situ growth of Ag nanoparticles on α-Ag2WO4 under electron irradiation: probing the physical principles, Nanotechnology 27 (2016) 225703, https://doi.org/10.1088/0957-4484/27/22/225703.
[107] J.C. Sczancoski, S. Maya-Johson, W. da Silva Pereira, E, Longo, E.R. Leite, Atomic diffusion induced by electron-beam irradiation: an in situ study of Ag structures grown from α-Ag2WO4, Cryst. Growth Des. 19 (2019) 106–115, https://doi.org/10.1021/acs.cgd.8b01076.
[108] G. Botelho, J.C. Sczancoski, J. Andres, L. Gracia, E. Longo, Experimental and theoretical study on the structure, optical properties, and growth of metallic silver nanostructures in Ag3PO4, J. Phys. Chem. C 119 (2015) 6293–6306, https://doi.org/10.1021/jp512111v.
[109] G. Wulff, XXV. Zur Frage der Geschwindigkeit des Wachsthums und der Auflösung der Krystallflächen, Z. Für Krist. - Cryst. Mater. 34 (1901) 449–530, https://doi.org/10.1524/zkri.1901.34.1.449.
[110] M. Assis, A.C.M. Tello, F.S.A. Abud, P. Negre, L.K. Ribeiro, R.A.P. Ribeiro, S. H. Masunaga, A.E.B. Lima, G.E. Luz Jr., R.F. Jardim, A.B.F. Silva, J. Andrés, E. Longo, Bridging experiment and theory: morphology, optical, electronic, and magnetic properties of MnWO4, Appl. Surf. Sci. 600 (2022) 154081, https://doi.org/10.1016/j.apsusc.2022.154081.
[111] A.F. Gouveia, C.M. Aldao, M.A. Ponce, E.R. Leite, E. Longo, J. Andrés, The hinge morphology of SnO2 as multifunctional semiconductor: what we can learn from simulations, theory, and experiments, Appl. Surf. Sci. 622 (2023) 156904, https://doi.org/10.1016/j.apsusc.2023.156904.
[112] V. Teodoro, A.F. Gouveia, T.R. Machado, A.B. Trench, N. Jacomaci, M. Assis, G. E. Marques, M.D. Teodoro, M.A. San-Miguel, J. Andrés, J. Bettini, E. Longo, Connecting morphology and photoluminescence emissions in β-Ag2MoO4 microcrystals, Ceram. Int. 48 (2022) 3740–3750, https://doi.org/10.1016/j.ceramint.2021.10.156.
[113] R. Alvarez-Roca, A.F. Gouveia, C.C. de Foggi, P.S. Lemos, L. Gracia, L.F. da Silva, C.E. Vergani, M. San-Miguel, E. Longo, J. Andrés, Selective synthesis of α-, β-, and γ-Ag2WO4 polymorphs: promising platforms for photocatalytic and antibacterial materials, Inorg. Chem. 60 (2021) 1062–1079, https://doi.org/10.1021/acs.inorgchem.0c03186.
[114] W. Tu, W. Guo, J. Hu, H. He, H. Li, Z. Li, W. Luo, Y. Zhou, Z. Zou, State-of-the-art advancements of crystal facet-exposed photocatalysts beyond TiO2: design and dependent performance for solar energy conversion and environment applications, Mater. Today 33 (2020) 75–86, https://doi.org/10.1016/j.mattod.2019.09.003.